Trace Element Effects on Precipitation Processes and Mechanical Properties in an Al-Cu-Li Alloy

D.L. GILMORE and E.A. STARKE, Jr.

A study has been made of how impurities (Na and K) and trace additions of indium, magnesium, and silicon affect the microstructure and related mechanical properties of an Al-Cu-Li alloy. Transmission electron microscopy (TEM) was used to determine the size and distribution of particles in four alloys. Indium and magnesium are both seen to stimulate T_1 precipitation. Indium also modifies θ" morphology, and magnesium greatly increases the number density of θ" precipitates. Strain localization was observed in underaged Al-Cu-Li-In tensile samples, consistent with observed changes in precipitate structure. No superposition of the effects of indium and magnesium was seen. High-resolution analytical microscopy was used to inspect precipitates for segregation of trace elements during early stages of aging, but no segregation was found within the detection limits of the system. Variations in heat treatment were made in order to study nucleation kinetics and trace element interactions with vacancies. Indium, with a binding energy less than that of lithium, was not seen to interact with quenched-in vacancies, while magnesium, with a binding energy greater than that of lithium, had a strong interaction. Yield anisotropies and fracture toughnesses were measured. Removal of trace impurities of sodium and potassium correlated with improved fracture properties. Magnesium was observed to increase anisotropy, especially in the T8 temper. A model was used to explain the anisotropy data in terms of texture and precipitate distribution.

I. INTRODUCTION AND BACKGROUND

MANY age-hardenable aluminum alloys are deformed prior to aging in order to introduce dislocation structures which will act as heterogeneous nucleation sites for precipitation. A stretch may also be applied to redistribute residual stresses. However, some product forms do not lend themselves readily to the use of this T8 temper. Alternatively, certain trace alloying additions have been shown to aid in the nucleation and/or growth of the strengthening phases.

There are several ways in which trace elements might alter the nucleation process:[1,2] they may shift the solvus or metastable solvus boundaries; they may reduce the interfacial energy associated with an embryo by segregating to the precipitate-matrix interface; or if the additions form a new particle, they may reduce the surface energy of a nucleating phase by providing a heterogeneous nucleation site. By interaction with vacancies, the solute may affect diffusion and the formation of clusters and dislocation loops which serve as nucleation sites. Finally, trace additions may affect the stability of a phase by changing the electron-to-atom ratio.

Uniaxial yield strength is not the only mechanical property of a material that may change with variations in the precipitation process. In textured products such as sheet, phases may have different effects on the anisotropy due to their orientation relationship with the matrix.[3–7] Thus, if a trace element changes the volume fraction of a precipitate, it may increase or decrease the anisotropy. Also, changes in precipitate size or morphology may lead to a change in deformation mechanism from shearing to looping. This will affect strain localization and related properties such as fatigue.[8]

The first work on trace additions in age-hardenable aluminum alloys was published by Sully *et al.*[9] They reported that the addition of 0.05 wt pct Sn to a commercial-purity Al-4.5Cu alloy resulted in a much lower response to natural aging but a marked increase in mechanical properties after artificial aging. Hardy[10,11] went on to examine the influence of the elements closely adjacent to tin on the periodic table. He found that small additions (~0.012 at. pct) of Cd or In had the same general effects in high-purity Al-4Cu and Al-4Cu-0.15Ti alloys. The increase in both the rate of aging and the peak strength was found to be significant at both 130 °C (403 K) and 190 °C (463 K), although the effect was much larger for the higher aging temperature. Cold work was found to interfere with trace alloying effects. Cadmium was also shown to reduce the specific interfacial enthalpy for θ' by a factor of roughly 6[12] in a similar Al-4Cu alloy. Interaction between trace solute atoms and vacancies was hypothesized to be responsible for suppression of Guinier–Preston (GP) zone formation during natural aging.[13]

Sankaran and Laird[14] provided evidence for the presence of what they believed to be trace-element-rich particles at the edges of θ' plates after aging an Al-4Cu alloy for 6 hours at 250 °C (523 K). A subsequent study of a similar alloy using energy dispersive X-ray microanalysis in a TEM also showed heterogeneous precipitation of θ' on very fine In particles after aging at 200 °C (473 K) for 1 minute.[15] Precipitation of θ' has also been observed on dislocation loops that were linked to Cd additions.[16] Silcock *et al.*[17] found anomalous X-ray diffraction spots which they attributed to trace-element-rich phases. Recent work by

D.L. GILMORE, Research Fellow, is with the Department of Materials, Oxford Centre for Advanced Materials and Composites, Oxford University, Oxford OX1 3PH, United Kingdom. E.A. STARKE, Jr., University Professor, is with the Department of Materials Science and Engineering, University of Virginia, Charlottesville, VA 22903.

Manuscript submitted December 13, 1996.

Table I. Chemical Composition of Alloys Studied

Alloy Designation	Cu	Li	Mg	Zr	In	Fe	Si	Al
Wt pct								
Al-Cu-Li	4.01	1.24	—	0.16	—	0.05	0.04	balance
Al-Cu-Li-In	4.06	1.21	—	0.16	0.09	0.05	0.04	balance
Al-Cu-Li-Mg	4.22	1.31	0.54	0.16	—	0.05	0.04	balance
Al-Cu-Li-Mg-In	4.30	1.32	0.55	0.15	0.086	0.05	0.04	balance
Al-Cu-Li, clean	4.30	1.18	—	0.14	—	0.01	0.01	balance
Al-Cu-Li-In, clean	4.23	1.12	—	0.14	0.08	0.02	0.01	balance
At. pct								
Al-Cu-Li	1.68	4.78	—	0.048	—	0.02	0.04	balance
Al-Cu-Li-In	1.71	4.65	—	0.048	0.02	0.02	0.04	balance
Al-Cu-Li-Mg	1.76	5.04	0.59	0.048	—	0.02	0.04	balance
Al-Cu-Li-Mg-In	1.81	5.07	0.61	0.044	0.020	0.02	0.04	balance
Al-Cu-Li, clean	1.82	4.55	—	0.040	—	0.005	0.01	balance
Al-Cu-Li-In, clean	1.80	4.32	—	0.040	0.02	0.01	0.01	balance

Ringer *et al.*[18] has used atom probe field ion microscopy to identify Sn-rich particles at the edges of θ' plates in an Al-4Cu alloy.

The first commercial Al-Cu-Li alloy, manufactured by ALCOA (Alcoa Center, PA) as 2020, used Cd to enhance θ' precipitation.[19] LeBaron[20] showed that the strength of Al-Cu-Li alloys increases with minor additions of a variety of elements, primarily Cd, but also including Zn, Hg, Ag, Sn, and In. The nominal composition of 2020 was Al-4.5Cu-1.1Li-0.5Mn-0.2Cd, and the major strengthening phase was θ'.

Silcock[21] pointed out that Cd did not affect precipitation of T_1, δ', or θ' at 165 °C (438 K) in Al-Cu-Li alloys where the Li content was relatively high (~2 to 3 wt pct). The X-ray spots associated with Cd precipitates in the Al-Cu binary system were not found in these alloys nor in Al-Li binary alloys. This is supported by the more recent work of Blackburn and Starke,[22] where Cd and Sn additions in the Al-Li-Cu alloy 2090 were not seen to affect the aging behavior. However, In was seen to enhance the uniform precipitation of both θ' and T_1 in this system. Mukhopadhyay *et al.*[2] found evidence of In-rich particles associated with T_1 plates in a 2090 sample aged at 250 °C (523 K) for 5 minutes.

In addition to In and Cd, Mg has long been known to increase the yield strength of Al-Cu alloys, especially in the naturally aged condition.[23,24] This effect has been attributed to the large Mg-vacancy binding energy.[25] Magnesium has also been found to be associated with T_1 and Ω precipitation in more complex systems.[18] Other trace elements which are present in commercial alloys as impurities can also affect the final properties. Silicon has been measured to have a significant binding energy with vacancies and thus must be considered to have a possible influence on precipitation.[25] The work of Hardy showed that the efficacy of Cd at suppressing natural aging in a commercial purity Al-4Cu-0.15Ti alloy was much less than in a high-purity sample.[11] Low levels of K or Na have been shown to lead to poor fracture behavior, perhaps due to the formation of brittle grain-boundary phases.[26]

Due to the complexity of the possible interactions that trace additions may have on the precipitation processes, it is not surprising that there have been conflicting reports in the literature regarding effects in various alloy systems. It is important to consider that a trace element may play differing roles in different phases, even within the same alloy. Although the topic of trace alloying additions to aluminum alloys has been studied for almost 50 years, the exact mechanisms responsible for the catalytic effect of many trace elements are still undetermined. Consequently, no decisive rules are available to predict which trace element may be chosen for a specific purpose.

II. EXPERIMENTAL PROCEDURE

A. *Materials and Processing*

ALCOA provided nominally 3.2-mm-thick rolled sheet of four Al-Cu-Li alloys. Comalco (Melbourne, Australia) provided two cylindrical Al-Cu-Li ingots with ultralow impurity levels produced by the VACLITE* process,[26] 127-mm diameter by 254-mm high. These ingots were subsequently homogenized in a molten salt bath at 516 °C (789 K) for 24 hours (following a slow heatup to avoid localized eutectic melting) and warm rolled to produce sheet material similar to that provided by ALCOA. The rolling process entailed seven passes at 427 °C (700 K) (two reheats) with a nominal true strain of 277 pct (94 pct reduction). The chemical compositions are listed in Table I. Additionally, both of the clean alloys contained less than 0.5 ppm sodium, 0.04 ppm potassium, and 0.25 ppm hydrogen.

*VACLITE is a trademark of COMALCO, Melbourne, Australia.

B. *Microstructural Evaluation*

Microstructures were characterized by optical metallography, scanning electron microscopy (SEM), transmission electron microscopy (TEM), and X-ray pole figure analysis. Due to the lithium content of the alloys studied, samples for observation were kept in vacuum desiccators when not in use in order to prevent corrosion.

Grain structure was investigated by optical microscopy. Samples were polished to 2400 grit with SiC paper, to 0.3 μm with alumina powder, and a final polish was done with a colloidal silica suspension. Etching was performed with Keller's reagent. Observations of fracture surfaces were made using a JSM-840 scanning electron microscope op-

erating at 20 and 35 kV. Energy dispersive X-ray spectra of regions on the fracture surfaces were obtained and analyzed using a KEVEX* microanalysis system.

*KEVEX is a trademark of Kevex Corporation, Foster City, CA.

Subgrain and precipitate structures were investigated using conventional (PHILIPS* EM400 or JEOL** JEM-2000FXII, operating at 120 kV and 200 kV respectively) and high-resolution (JEOL JEM-4000EX operating at 400 kV or JEM-2010F at 200 kV) TEM. The TEM samples were prepared by mechanical thinning with SiC paper to 150 μm followed by electropolishing with an applied potential of 15 V in a 3:1 methanol-nitric acid solution cooled to −25 °C (248 K). Low-temperature ion milling (13 deg angle of incidence, 4 kV, 0.5 mA, 20 to 30 minutes) was used for further thinning of samples for high-resolution work.

*PHILIPS is a trademark of Philips Electronic Instruments Corp., Mahwah, NJ.

**JEOL is a trademark of Japan Electron Optics Ltd., Tokyo.

In addition to qualitative TEM observations, stereology was done to determine volume fraction, number density, diameter, and thickness of the strengthening phases. Analysis followed that of Underwood.[27] Although Underwood does not specifically consider the case of oriented plate-shaped particles in a thin-foil projection, the formula for the volume fraction of particles (corrected for truncation and overlap) was determined to be

$$V_V = \left(\frac{-2\pi d}{\pi d + 8h}\right) \ln (1 - A_A) \qquad [1]$$

where d is the plate diameter, h is the foil thickness, and A'_A is the projected area fraction of precipitates, determined by the point count method. Foil thicknesses were measured *via* convergent beam electron diffraction patterns.[28]

High-resolution energy dispersive X-ray spectral data were collected on the 2010 field-emission gun transmission electron microscope. Probe sizes down to 0.5 nm were used. The take-off angle was approximately 25 deg. Collection times ranged from 40 to 180 seconds. Precipitates were oriented edge-on to the foil surface. Data were analyzed using the DTSA software package (Standard Reference Data Program, 221/A323, NIST, Gaithersburg, MD, 20899) . Comparisons were made between precipitate spectra and matrix spectra collected under similar conditions. Computer-generated spectra were also employed as references.

X-ray diffraction data were taken on a goniometer from $\alpha = 0$ to 80 deg using center sections of as-quenched samples. (111), (200), and (220) poles were analyzed with the popLA software package.[29] The program was used to convert the pole-figure data into an orientation distribution function (ODF) for each alloy. From these ODFs, theoretical Taylor factors were calculated as a function of the tensile axis-rolling direction angle, assuming restricted glide.

C. *Mechanical Testing*

Initial optimization of the heat treatment was performed using an Indentron Rockwell hardness testing system. Samples approximately 25-mm square were solutionized in a muffle furnace at 530 °C (803 K) for 1 hour followed by a cold-water quench. Samples were then aged at temperatures ranging from 120 °C to 190 °C (393 to 463 K) in a circulating air furnace, wax bath, or oil bath. Curves of hardness (Rockwell A, B, or D scale) *vs* aging time guided subsequent mechanical tests.

Tensile tests were performed on the material using standard subsize specimens as dictated by ASTM E8. Sample gage lengths were 25.4 mm with a width of 6.35 mm and a nominal thickness of 3.2 mm. Strain rates were approximately 10^{-3} s^{-1}. Tests were performed on specimens cut at 0, 45, and 90 deg to the rolling direction for various aging periods and pre-stretches from 0 to 6 pct. As-quenched samples were kept at −196 °C (77 K) to ensure that no natural aging occurred before testing. Yield strength (0.2 pct offset), tensile strength, work-hardening exponent (estimated to be the true strain at necking), and elongation to fracture were measured for each specimen. A few tests were interrupted after elongations of 2 or 4 pct, and TEM samples were taken from the sample gage lengths for investigation of deformation mechanisms.

The R curves were used to assess the fracture toughness of the alloys. Testing was conducted according to ASTM E561, using potential-drop methodology to measure crack length. The data were analyzed to determine plane-strain fracture toughness at crack initiation (K_{JIC}) as well as the usual K_Q.[30] The L-T oriented compact-tension specimens employed were 38.1-mm wide and nominally 3.2-mm thick. Precracking was performed at five cycles per second.

Experiments were also conducted to determine if the trace elements in these alloys interacted with quenched-in vacancies. Identical samples were either quenched into a cold-water bath from the solution heat treatment temperature and then aged in a wax bath at 160 °C (433 K) or quenched directly into the wax bath and aged. Hardness curves were also measured for natural aging of all six alloys.

In order to study possible shifts in metastable phase boundaries, two double aging experiments were carried out. In one, specimens were aged first at 120 °C (393 K) for 20 hours and then for a series of times at 160 °C (433 K). In the other, specimens were aged first at 160 °C (433 K) for a series of times and then aged for approximately 160 hours at 120 °C (393 K).

III. RESULTS

A. *Grain Structure*

Optical metallography of the alloys revealed an unrecrystallized grain structure with large, elongated, pancake-shaped grains, approximately 1500-μm long by 250-μm wide. There were no significant differences in grain structure with changes in alloy composition, although the subgrains in the Al-Cu-Li and Al-Cu-Li-In alloys are approximately 3 times larger than those in the magnesium-bearing alloys (2 μm *vs* 0.6 μm). The subgrains are equiaxed in all alloys.

A representative (200) X-ray pole figure taken from an as-quenched Al-Cu-Li sample is shown in Figure 1. The primary texture component is copper, approximately 15 to 25 times random, with some brass component present as well. The differences in texture between the alloys were not

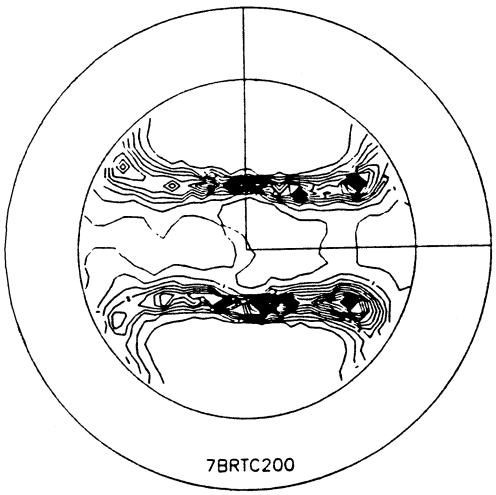

Fig. 1—(200) X-ray pole figure from midplane of as-quenched Al-Cu-Li sample.

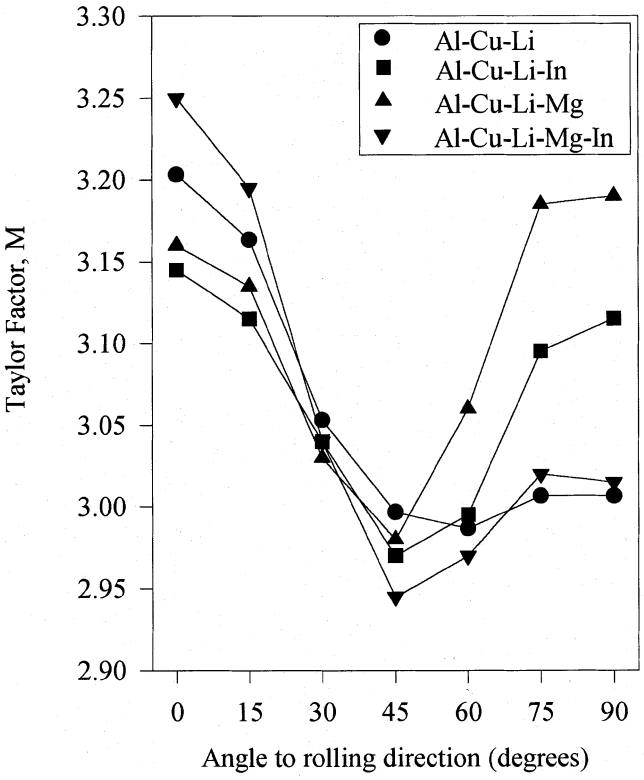

Fig. 2—Taylor factors calculated from as-quenched X-ray pole figure data.

large. Theoretical Taylor factors were calculated with the popLA software package[29] from the texture data using an assumption of full constraint and are graphed as functions of the angle to the rolling direction in Figure 2. Calculations for a similar system have shown that the differences between an assumption of fully constrained or less-constrained pancake-shaped grains are not large.[31] Thus, these Taylor factors should be roughly proportional to the as-quenched yield anisotropies of the alloys.

B. *Properties and Precipitate Microstructures*

The following sections detail the microstructures and mechanical properties of the alloys for a variety of aging conditions. All tensile results are averages of at least two tests. Specimen geometries are listed relative to the rolling direction of the sheet. A ''+'' after the strain-to-failure value indicates that one or more of the samples underwent necking outside of the region measured by the strain gage.

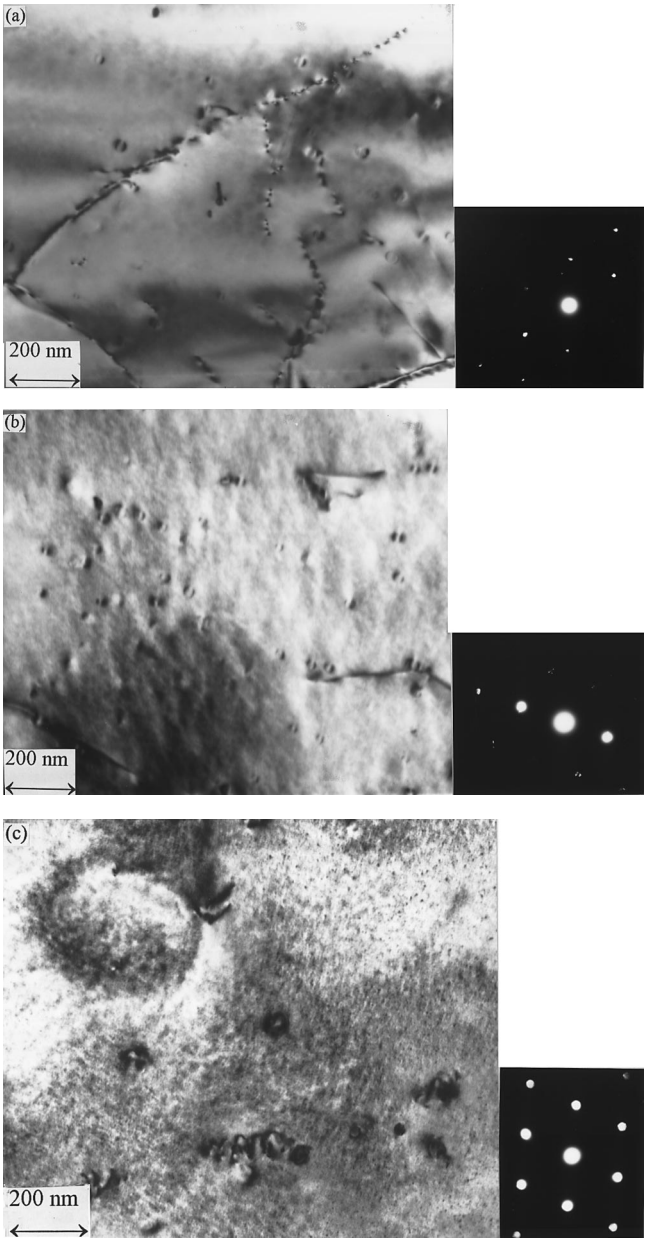

Fig. 3—As-quenched sheet microstructures of (*a*) Al-Cu-Li, (*b*) Al-Cu-Li-In, and (*c*) Al-Cu-Li-Mg. Bright-field TEM images, [110] beam axis.

1. *As-quenched*

Figures 3(a) and (b) indicate the as-quenched microstructures of the Al-Cu-Li and Al-Cu-Li-In alloys. The β' (Al_3Zr) phase, identified by X-ray microanalysis, is the only phase evident, although some short dislocation segments are also present. Figure 3(c) is representative of the as-quenched microstructure of the Mg-containing alloys. The mottled background contrast and diffraction streaks along the {100} direction are evidence of Al-Cu GP zone formation. Dislocation loops and helices are also seen. These micrographs agree with the large natural aging response of

the Mg-bearing alloys plotted in Figure 4. Table II lists the yield strength (σ_{YS}), ultimate tensile strength (σ_{UTS}), work-hardening exponent (n), and engineering strain to fracture (ε_F) for all alloys in the as-quenched condition.

The interaction of trace element additions with quenched-in vacancies may be inferred from the effect of quench temperature on aging. Aging in the Mg-free alloys is significantly retarded by quenching to the aging temperature of 160 °C (433 K) rather than using a standard cold-water quench; the hardnesses were lowered by two to four standard deviations (depending upon aging time) in the baseline alloy and by three to five standard deviations in the Al-Cu-Li-In alloy. Conversely, aging in the Mg-bearing alloys is relatively unaffected by the change in the quench temperature. In a separate experiment, no difference was seen in the aging of any alloy when the quench was changed from iced brine to room temperature water.

2. *Aging at 120 °C (393 K)*

Rockwell hardness *vs* aging time at 120 °C (393 K) is plotted in Figure 5 to show the effect of In and Mg on aging. Indium appears to slightly retard aging relative to the baseline alloy, while the Mg-containing alloys display a larger initial aging response. After approximately 20 hours, the rates of aging do not differ greatly. Representative microstructures of the Mg-containing and Mg-free alloys after 20 hours at 120 °C (393 K) are shown in Figure 6. Indium does not seem to notably affect the microstructure at this aging temperature. The yield strengths of the alloys after 20 hours at 120 °C (393 K) are 269 MPa for the baseline alloy, 262 MPa for Al-Cu-Li-In, 316 MPa for Al-Cu-Li-Mg, and 320 MPa for Al-Cu-Li-Mg-In.

3. *Double aging experiments*

Evidence that In affects precipitation kinetics is provided by the results of the two double-aging experiments in Figure 7. In the first experiment, Al-Cu-Li and Al-Cu-Li-In samples were ''preaged'' for 20 hours at 120 °C (393 K). Hardness data for subsequent aging at 160 °C (433 K) are shown in Figure 7(a). First, reversion associated with dissolution of GP zones is observed, followed by rapid divergence of the In and baseline aging response. In the second experiment, samples were first preaged at 160 °C (433 K) for 0, 2, 4, or 6 hours, then all samples were aged for 160 hours at 120 °C (393 K). The high-low aging data in Figure 7(b) show that In primarily affects the nucleation or the very early stages of precipitate growth. With no high-temperature exposure, the two alloys show identical aging behavior at 120 °C (393 K). However, only a short exposure at 160 °C (433 K) is necessary for aging to be significantly increased in the Al-Cu-Li-In relative to the baseline alloy, even though the bulk of the thermal energy input is at 120 °C (393 K). Comparison of aging in the baseline and Al-Cu-Li-In alloys at a range of temperatures indicates that the boundary for an effect of In on aging is between 130 °C and 140 °C (403 to 413 K).

4. *Aging at 160 °C—tensile properties and microstructures*

Contrary to the behavior observed at 120 °C (393 K), In has a pronounced effect on the aging of the baseline alloy at 160 °C (433 K), as shown in Figure 8. The Al-Cu-Li-In alloy has a T6 yield strength approximately 25 pct higher than that of the baseline alloy, and the time to peak age is

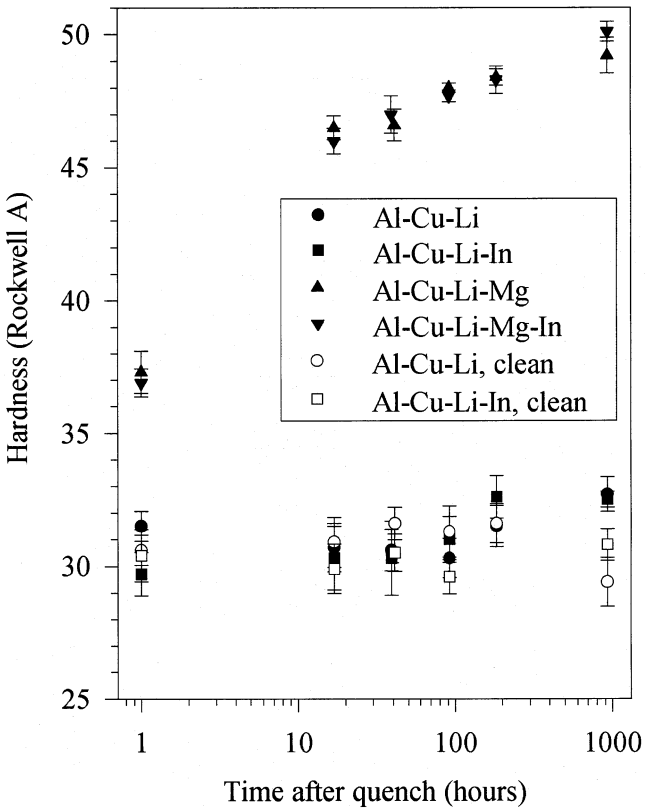

Fig. 4—Natural aging of sheet material. Hardness *vs* time after solution heat treatment.

cut by roughly 75 pct. For an aging time of 24 hours, the In-containing alloy has a yield strength about 70 pct higher than that of the In-free alloy. Magnesium is also observed to accelerate and increase the aging response, but no superposition of the Mg and In effects are seen. Rather, the Al-Cu-Li-Mg-In alloy is consistently slightly weaker than the Al-Cu-Li-Mg.

When impurity contents (probably associated with Si) of the Al-Cu-Li and Al-Cu-Li-In alloys are reduced, the time to reach peak hardness in the sheet material is increased, but the magnitude of the In effect is not greatly changed. The vacuum-refined, low-impurity (''clean'') material also exhibits the In-strengthening effect but does not reach quite as high a strength as the conventional-purity alloys. Peak strength in the clean Al-Cu-Li-In alloy is achieved by aging at 175 °C (448 K), higher than for the other alloys. Data for the low-impurity material contained considerably more variability than data obtained from the original four alloys, perhaps due to differences in the casting and rolling processes.

Table III summarizes the peak-aged yield strength data for the six alloys along with the peak-strength heat treatments. Note that the temper designations T83 and T86 are used here to indicate longitudinal stretches of 3 pct and 6 pct, respectively, prior to aging. The Al-Cu-Li-In alloy does not benefit appreciably from cold work prior to aging as do the other alloys. The Al-Cu-Li-In T6 temper (no cold work prior to aging) has mechanical properties roughly equivalent to those of the Al-Cu-Li T86 temper, but it requires one-third less aging time at 160 °C (433 K). While the Al-Cu-Li-Mg alloy displays the highest strength of the four,

Table II. As-Quenched Sheet Tensile Properties

Composition	Geometry	σ_{YS} (MPa)	σ_{UTS} (MPa)	ε_F (Pct)	n
Al-Cu-Li	longitudinal	152	354	22+	0.197
	45 deg to RD	143	355	24	0.193
	transverse	155	334	16	0.138
Al-Cu-Li-In	longitudinal	145	356	25	0.197
	45 deg to RD	140	340	23	0.179
	transverse	152	343	19	0.163
Al-Cu-Li-Mg	longitudinal	160	402	19+	0.171
	45 deg to RD	154	426	28	0.235
	transverse	168	417	20+	0.184
Al-Cu-Li-Mg-In	longitudinal	157	419	27	0.232
	45 deg to RD	156	416	29	0.227
	transverse	165	408	20+	0.184
Al-Cu-Li, clean	longitudinal	150	389	23	0.184
	45 deg to RD	134	371	32	0.236
	transverse	144	381	26+	0.188
Al-Cu-Li-In, clean	longitudinal	138	344	22	0.176
	45 deg to RD	130	336	28	0.202
	transverse	138	346	22+	0.178

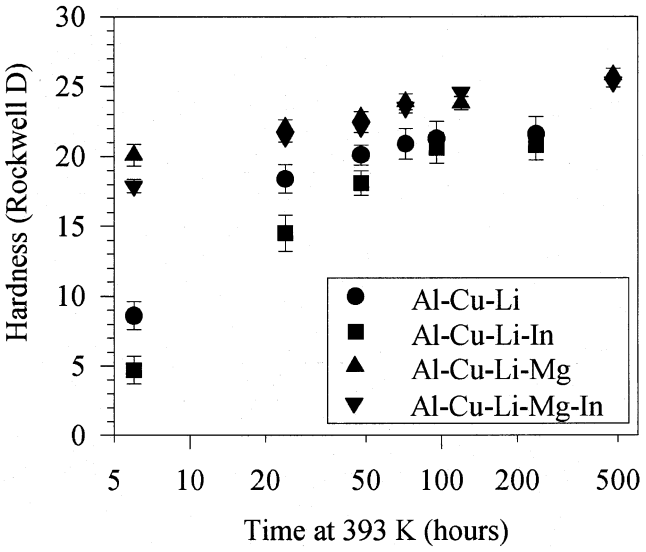

Fig. 5—Effect of trace additions on the aging behavior of Al-Cu-Li at 393 K.

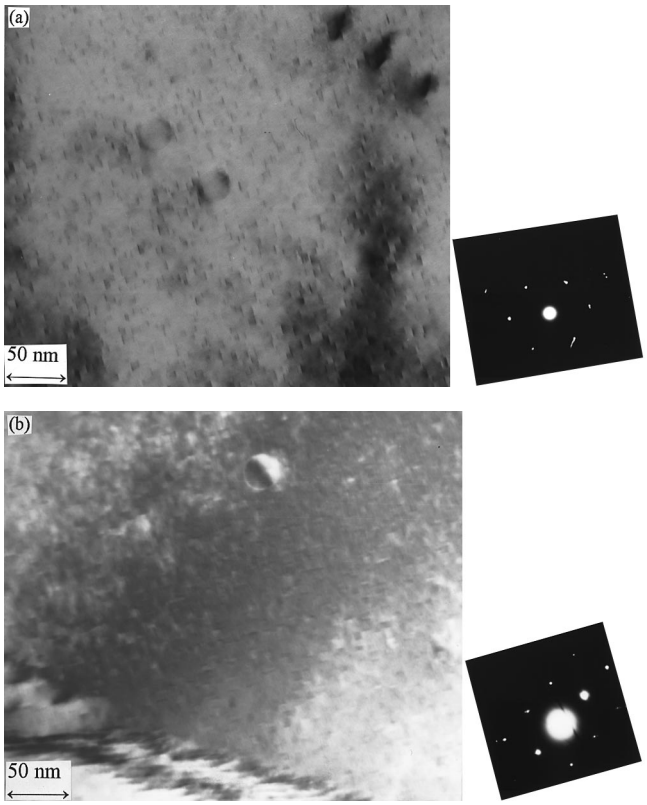

Fig. 6—Alloy microstructures after 20 h at 393 K: (*a*) Al-Cu-Li and (*b*) Al-Cu-Li-Mg. Bright-field TEM images, [110] beam axis.

aging time for the T6 temper is almost triple that for the Al-Cu-Li-In alloy.

5. *Strain localization behavior*

Figure 9 indicates the low-magnification dislocation microstructures present in the baseline and Al-Cu-Li-In alloys after aging for 5 and 20 hours at 160 °C (433 K). At 5 hours, when the yield strength of the alloys has just begun to diverge, In-containing alloy contains a few bands of high dislocation density, whereas the baseline alloy displays a more homogeneous deformation. At the later aging time, when the In alloy is close to peak strength, no notable difference in deformation microstructure can be seen.

6. *Early aging—high resolution TEM and microanalysis*

High resolution TEM was used to examine precipitates during the early stages of aging. Figures 10(a) and (b) show θ'' and θ' for the conventional-purity alloys after 5 hours at 160 °C (433 K). The corresponding longitudinal sheet yield strengths are 206 MPa for the Al-Cu-Li alloy and 296 MPa for the Al-Cu-Li-In alloy. Note the larger particle thickness for the In-bearing alloy. The Al-Cu-Li-In micrograph also shows what may be a dislocation connecting the θ' particles. No significant differences in T_1 structure were noted at early aging times among the various alloys. In samples aged for less than 5 hours at 160 °C (433 K), T_1 precipitates were observed primarily at subgrain boundaries.

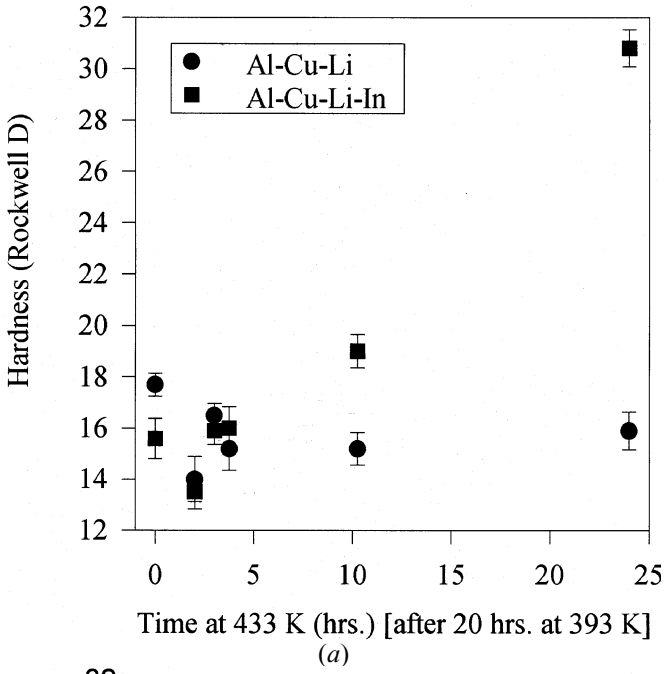

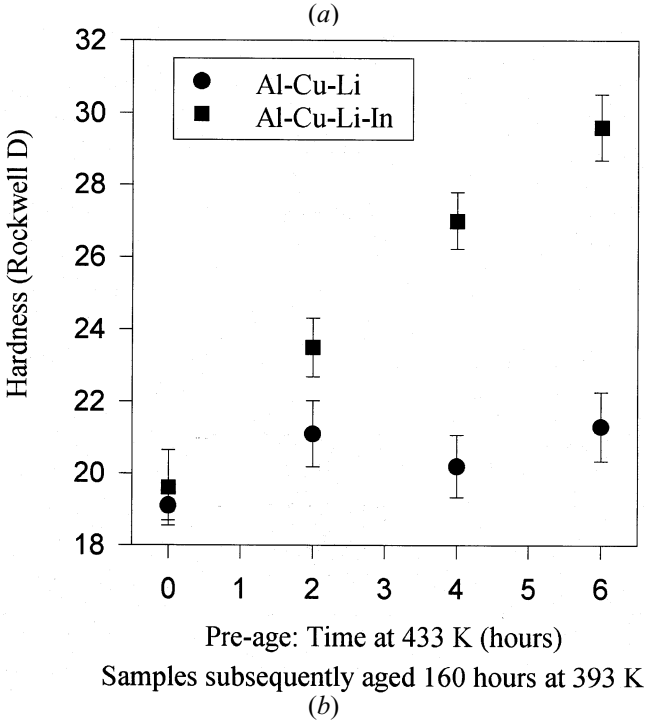

Fig. 7—(*a*) Low-high double aging of alloys—20 h at 393 K followed by varying times at 433 K. (*b*) High-low double aging of alloys—varying times at 433 K followed by 160 h at 393 K.

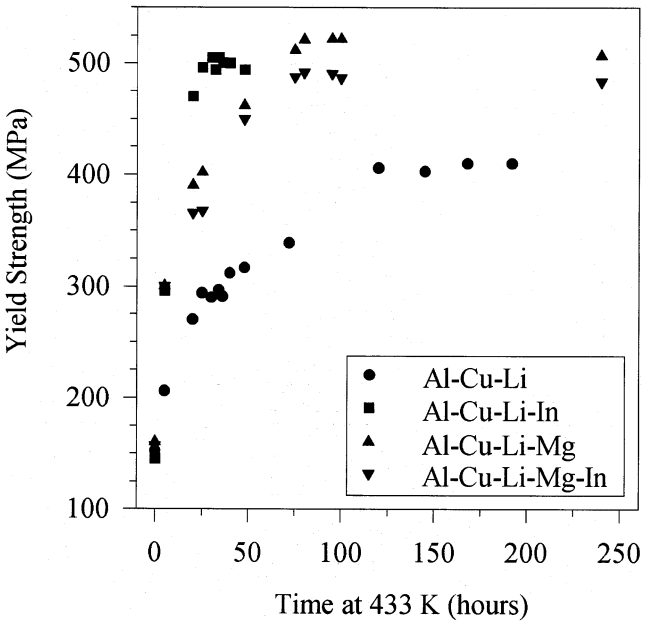

Fig. 8—Longitudinal tensile yield strengths *vs* aging time at 433 K. No preage stretch applied.

Table III. Sheet Peak Strength Heat Treatments

	Yield Strength (MPa)			Heat Treatment (h/°C)		
Composition	T6	T83	T86	T6	T83	T86
Al-Cu-Li	407	—	501	150/160	—	48/160
Al-Cu-Li-In	498	—	513	32/160	—	28/160
Al-Cu-Li-Mg	524	575	585	88/160	81/160	48/160
Al-Cu-Li-Mg-In	494	564	592	88/160	81/160	48/160
Al-Cu-Li, clean	402	—	—	144/160	—	—
Al-Cu-Li-In, clean	474	—	—	32/175	—	—

The fine probe capabilities of the 2010 field-emission gun transmission electron microscope were used to search for segregation of trace elements to precipitate interfaces or interiors. Probe sizes down to 0.5 nm diameter were used, but specimen drift over the time needed to collect a statistically significant number of counts led to a larger effective sampling area. Therefore, it was not possible to distinguish between the interface and interior of a given precipitate.

Despite an extensive search, no In peaks were found to be associated with T_1 or θ' precipitates in any of the alloys. Computer-generated spectra were used to estimate that 1.6 wt pct (0.4 at. pct) was the lowest concentration of In which might be distinguished from background noise. This would represent a 20-fold increase over the amount of In in the alloy as a whole. In the Mg-containing alloys, no Mg concentrations were found in the precipitates which were significantly higher than those associated with the surrounding matrix. It was not possible to search for Si concentrations in precipitates due to a silicon peak artifact present in all spectra collected. Spherical particles present through all tempers were found to be rich in Zr, confirming that they are β'. All other ''particles'' examined were found to be hydrocarbon-based contamination spots.

7. *Intermediate aging*

Figure 11 depicts the microstructures of the four conventional-purity alloys at an intermediate stage of aging. The micrographs were all taken after 20 hours at 160 °C (433 K), corresponding to yield strengths of 270 MPa (66 pct of T6) for Al-Cu-Li, 482 MPa (97 pct of T6) for Al-Cu-Li-In, 390 MPa (74 pct of T6) for Al-Cu-Li-Mg, and 366 MPa (74 pct of T6) for the Al-Cu-Li-Mg-In alloy.

The baseline Al-Cu-Li alloy is characterized by a fine distribution of θ'', changing slowly over to θ' as peak strength is approached. The T_1, identified from selected area diffraction patterns, is only observed at subgrain and grain boundaries, although it is present in the matrix to a slight extent in overaged samples. The Al-Cu-Li-In alloy is char-

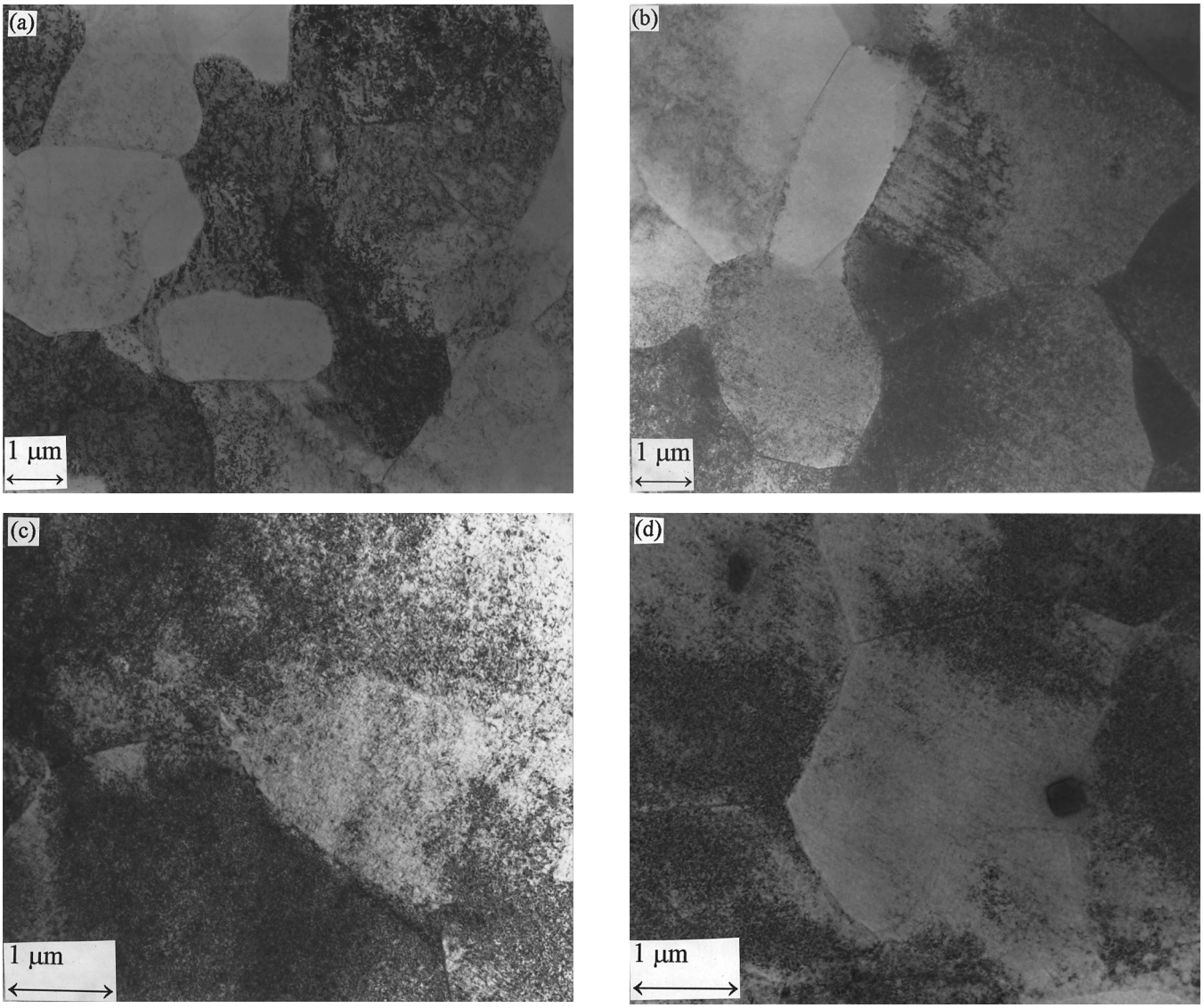

Fig. 9—Tensile deformation microstructures after aging at 433 K. (*a*) Al-Cu-Li, 5 h, 4 pct stretch; (*b*) Al-Cu-Li-In, 5 h, 2 pct stretch; (*c*) Al-Cu-Li, 20 h, 2 pct stretch; and (*d*) Al-Cu-Li-In, 20 h, 2 pct stretch.

acterized by homogeneous matrix precipitation of θ' particles (or very thick θ'') even after only 5 to 10 hours of aging at 160 °C (433 K). The number density of the θ' phase in the Al-Cu-Li-In is similar to that of θ'' in the baseline material, but the particles are thicker and shorter. However, the greatest differences in particle thickness were noted in samples aged less than 20 hours at 160 °C (433 K), and there was considerable scatter in the measurements at later times. The T_1 is also present in the matrix of the Al-Cu-Li-In alloy after 5 to 10 hours of aging at 160 °C (433 K), though in much lower numbers than θ'.

The two Mg-containing alloys have microstructures similar to one another, characterized by a very high number density of GP zones and θ'' precipitates. The T_1 is also present, more than in the Al-Cu-Li-In alloy, but still at a much lower number density than the θ''. The T_1 particles in Mg-bearing alloys tend to have higher aspect ratios than those in the Al-Cu-Li-In alloy.

8. *Peak aging (T6 and T8)*

The peak strength (T6) microstructures of the alloys display similar features to those observed after 20 hours of aging, although the particle sizes are larger. The β' was observed in all samples, remaining roughly constant in size during heat treatments. No S' or δ' was observed in any of the alloy tempers, although it is possible that some δ'/β' coprecipitation occurred. The dominant deformation mechanism at peak strength in all of the alloys is Orowan looping. The two clean alloys have microstructures fairly similar to their respective conventional-purity counterparts, although the particles in the clean alloys are somewhat more coarse and the alloys contain more T_1.

The microstructures for the T86 temper are shown in Figure 12. The relative fractions of θ' and T_1 are greatly changed from the T6 temper; the baseline and Al-Cu-Li-In alloys contain roughly equal amounts of θ' and T_1, while the alloys with Mg additions are strengthened almost entirely by T_1. Note that the micrographs in Figure 12 were taken at the peak strength for each alloy, which does not correspond to equivalent aging times.

Tables IV and V list the yield strength (σ_{YS}), ultimate tensile strength (σ_{UTS}), work-hardening exponent (n), and engineering strain to fracture (ε_F) for the sheet material in

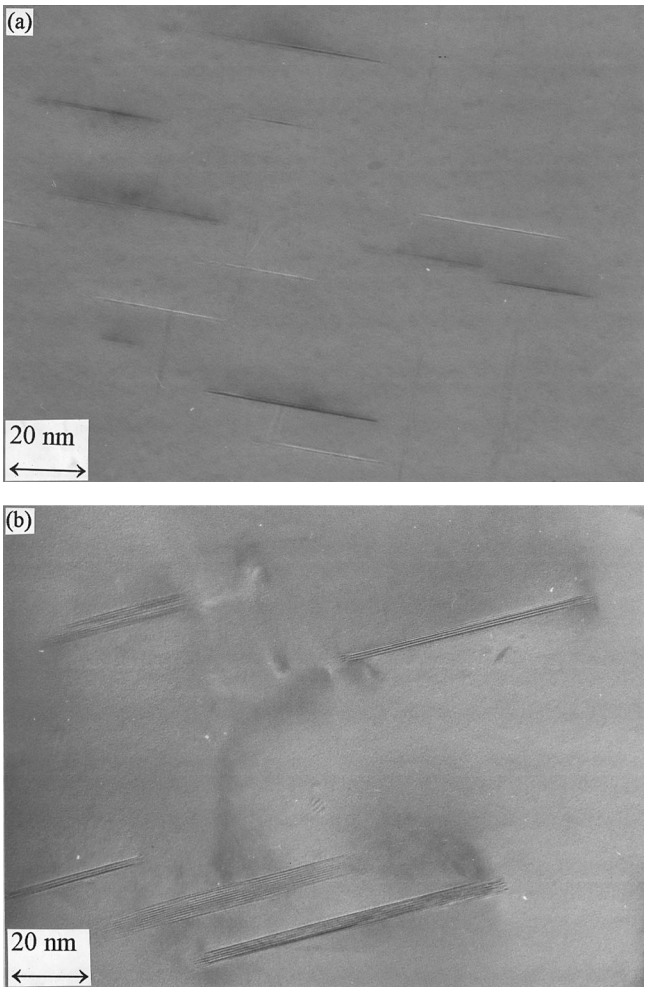

Fig. 10—High-resolution phase-contrast TEM images of θ'' in (*a*) Al-Cu-Li and (*b*) Al-Cu-Li-In. Both samples aged 5 h at 433 K. [100] beam axis.

the T6 and T86 conditions. Note the relatively large ductilities of the clean alloys for tensile testing at 45 and 90 deg to the rolling direction.

Table VI shows the tensile yield anisotrophy ratios for the six alloys, calculated by dividing the 45 deg and transverse yield strengths by the corresponding longitudinal yield strength for each composition and temper. Notably, both Mg-bearing alloys have higher anisotropies relative to the Mg-free alloys in the T6 and especially the T86 tempers. It should be noted, however, that the 45 deg yield strengths of the Al-Cu-Li-Mg are still higher than those of the other alloys. While the rolling processes were nominally the same for all alloys, the higher anisotropies in the relatively clean alloys may be due to differences in the casting process (rectangular slab ingot for the conventional-purity alloys and cylindrical ingot for the clean alloys). Recalling Figure 2, the Taylor factors calculated from texture data indicate differences in texture should only be reflected in the transverse yield anisotropies.

C. *Fracture Behavior*

In the T6 condition, longitudinal sheet tensile samples failed in plane stress by transgranular shear. No major differences among the alloys were noted in the longitudinal fracture behavior. Figure 13 shows a typical longitudinal fracture surface. Note that the fracture surface is tilted roughly 45 deg to the rolling plane.

Figure 14 displays the results of *R*-curve testing in the L-T orientation. The four alloys with higher impurity levels have fracture toughnesses that drop off roughly linearly with increasing yield strength. On average, significantly higher toughnesses were measured for the two alloys with low impurity levels, but there was more scatter in the data. Note that the K_{JIC} plane-strain fracture-initiation toughness values were determined from calculations of the total fracture energy as determined by ASTM E1152, combining the elastic and plastic energy terms, the latter being estimated by an area technique.[30]

IV. MODELING AND DISCUSSION

A. *Longitudinal Yield Modeling*

An attempt has been made to model the longitudinal yield strengths of the conventional purity sheet alloys. The model consists of two parts: a recent Orowan looping model developed by Nie *et al.*[32] and a shearing model by Brown and Ham.[33] Grain-boundary strengthening is assumed to be relatively small and constant throughout aging. This is reasonable, as the grain structure is stable, and the slip distances associated with the grains and subgrains are very large compared with the interparticle spacings. Solid solution strengthening is assumed to decrease as precipitation proceeds. The polycrystalline yield strength of the matrix after aging is calculated to be about 36 MPa in the Mg-free alloys and 45 MPa in the Mg-bearing alloys. This is 16 MPa for pure aluminum,[34] plus roughly 20 MPa for the 3 at. pct of Li that remains in solid solution,[35] plus roughly 9 MPa for the 0.5 at. pct of Mg in solution.[36]

1. *Orowan modeling*

Nie *et al.* developed an Orowan model for oriented plates or rods, which takes into account the three-dimensional nature of the precipitate habit planes. Their model grew out of earlier efforts by Kelly,[37] Merle *et al.,*[38] and Huang and Ardell.[39] For a distribution of plate-shaped precipitates on a specific set of planes, they calculate the increase in critical resolved shear stress to be

$$\Delta\tau = \frac{G\mathbf{b}}{2\pi(1-\nu)^{1/2}} \frac{1}{L_0} \ln\left(\frac{At}{r_0}\right) \qquad [2]$$

For the effective interparticle spacing, L_0, they use an equation similar to that for calculating the interparticle spacing for a distribution of spheres. However, they also take into account the geometry of the plate distribution:

$$L_0 = 0.931 \sqrt{\frac{B\pi dt}{V_v}} - \frac{\pi d}{8} - Ct \qquad [3]$$

where G, $\mathbf{b}$, and ν are the shear modulus, Burgers vector, and Poisson's ratio for the matrix phase (28 GPa, 0.286 nm, and 0.34); d, t, and V_v are the average diameter, thickness, and volume fraction of the precipitates determined by TEM stereology; and A, B, and C are geometric constants related to the precipitate habit planes (for {100} plates, they are 1.225, 0.306, and 1.061, and for {111} plates, they are

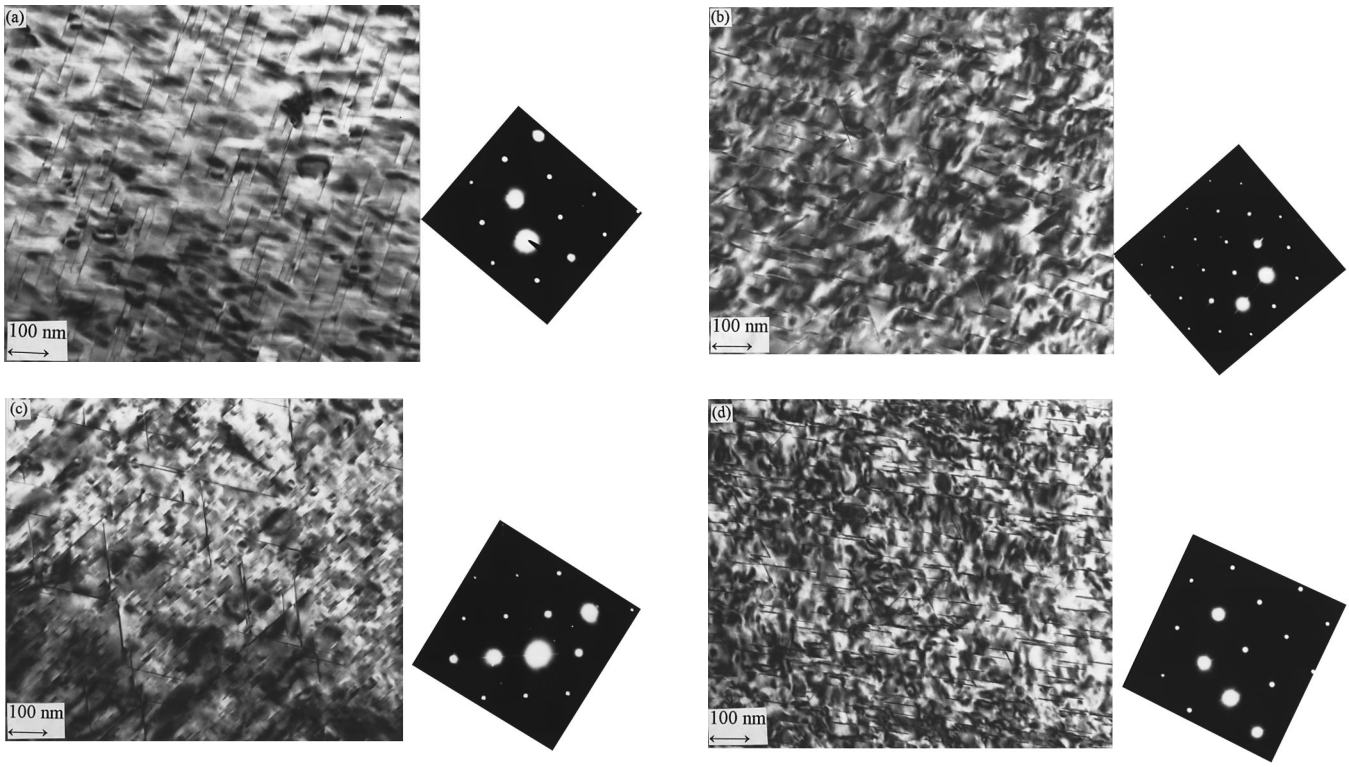

Fig. 11—Alloy microstructures after aging at 433 K for 20 h: (*a*) Al-Cu-Li, (*b*) Al-Cu-Li-In, (*c*) Al-Cu-Li-Mg, and (*d*) Al-Cu-Li-Mg-In. Bright-field TEM images, [110] beam axis.

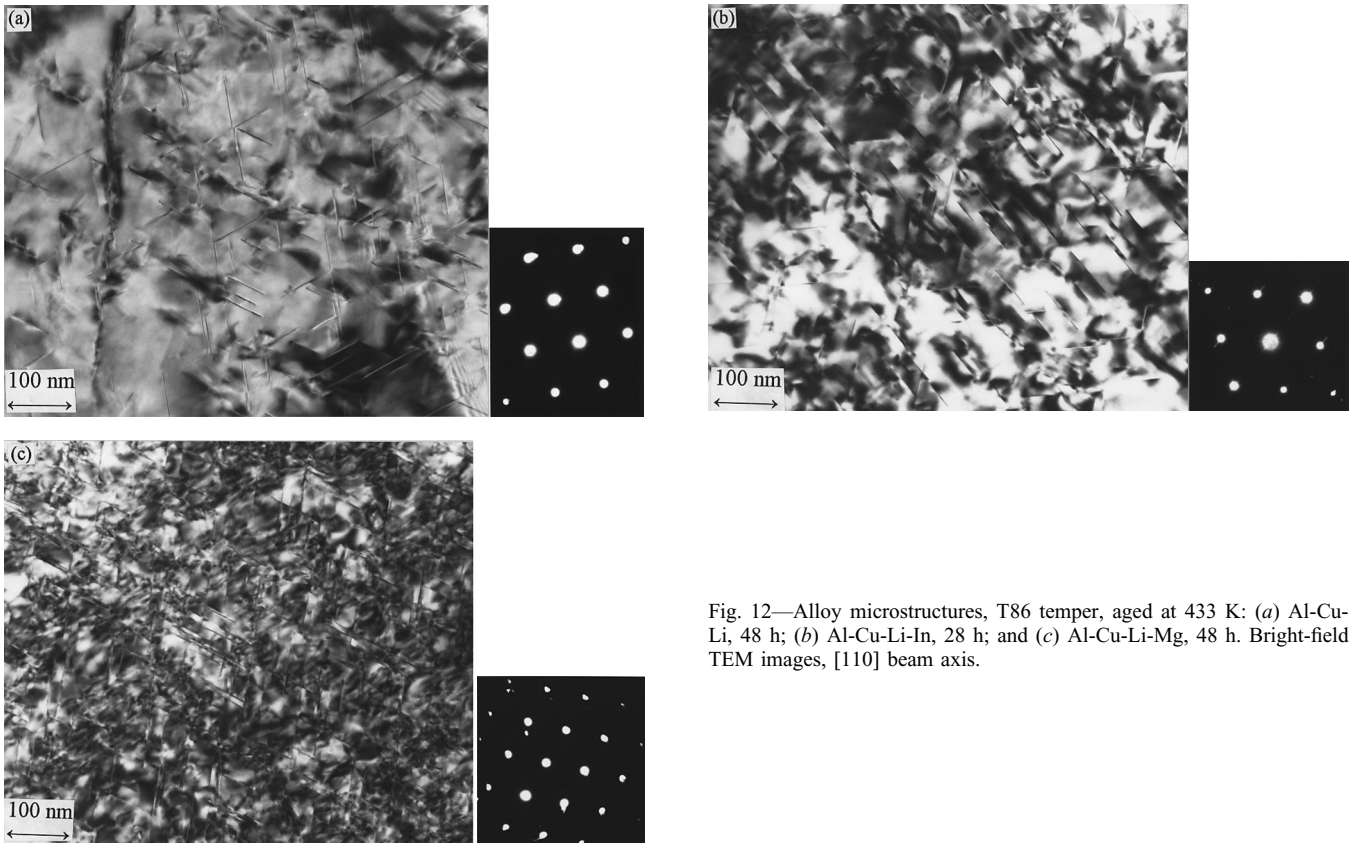

Fig. 12—Alloy microstructures, T86 temper, aged at 433 K: (*a*) Al-Cu-Li, 48 h; (*b*) Al-Cu-Li-In, 28 h; and (*c*) Al-Cu-Li-Mg, 48 h. Bright-field TEM images, [110] beam axis.

Table IV. Peak-Strength (T6) Tensile Properties

Composition	Geometry	σ_{YS} (MPa)	σ_{UTS} (MPa)	ε_F (Pct)	n
Al-Cu-Li	longitudinal	407	515	9	0.071
	45 deg to RD	390	478	5+	0.048
	transverse	403	444	1.5+	0.016
Al-Cu-Li-In	longitudinal	498	586	9	0.076
	45 deg to RD	483	540	5+	0.038
	transverse	486	508	1.5+	0.014
Al-Cu-Li-Mg	longitudinal	524	583	6	0.048
	45 deg to RD	491	564	6.5	0.054
	transverse	516	552	2	0.018
Al-Cu-Li-Mg-In	longitudinal	494	566	8	0.061
	45 deg to RD	465	546	7	0.061
	transverse	488	523	2	0.019
Al-Cu-Li, clean	longitudinal	402	530	8.5+	0.066
	45 deg to RD	377	500	10+	0.078
	transverse	407	522	6	0.054
Al-Cu-Li-In, clean	longitudinal	474	595	10	0.075
	45 deg to RD	396	504	12+	0.076
	transverse	414	520	8.5	0.069

Table V. T86 Tensile Properties

Composition	Geometry	σ_{YS} (MPa)	σ_{UTS} (MPa)	ε_F (Pct)	n
Al-Cu-Li	longitudinal	501	560	9	0.061
	45 deg to RD	486	560	8.5	0.058
	transverse	528	560	3+	0.026
Al-Cu-Li-In	longitudinal	513	581	8.5	0.065
	45 deg to RD	504	550	3.5+	0.035
	transverse	534	556	2	0.014
Al-Cu-Li-Mg	longitudinal	585	618	3.5	0.031
	45 deg to RD	518	557	2	0.022
	transverse	549	562	1	0.010
Al-Cu-Li-Mg-In	longitudinal	592	614	2	0.020
	45 deg to RD	529	554	1.5+	0.014
	transverse	546	559	1	0.010

Table VI. Yield Anisotropy Ratios

	As-Quenched		T6		T86	
Composition	σ_{45}/σ_0	σ_{90}/σ_0	σ_{45}/σ_0	σ_{90}/σ_0	σ_{45}/σ_0	σ_{90}/σ_0
Al-Cu-Li	0.938	1.018	0.958	0.990	0.971	1.053
Al-Cu-Li-In	0.960	1.050	0.970	0.978	0.982	1.042
Al-Cu-Li-Mg	0.959	1.046	0.938	0.985	0.885	0.938
Al-Cu-Li-Mg-In	0.992	1.051	0.942	0.989	0.894	0.923
Al-Cu-Li, clean	0.900	0.960	0.913	1.012	—	—
Al-Cu-Li-In, clean	0.939	1.000	0.836	0.872	—	—

1.061, 0.265, and 0.919, respectively). The inner cut-off radius for dislocation energy calculations, r_0, is assumed to be equal to 2**b**, following Kelly.

2. *Shearing model*

A coherency strain model has been used to estimate the strengthening component due to sheared θ'' or θ' particles at early stages of aging. Models of modulus and chemical strengthening were also considered, but found to give wildly unrealistic predictions. The strain model used is taken directly from Brown and Ham:

$$\Delta\tau = 4.1\ G\ |\varepsilon|^{3/2} \left(\frac{V_v d}{2\mathbf{b}}\right)^{1/2} \qquad [6]$$

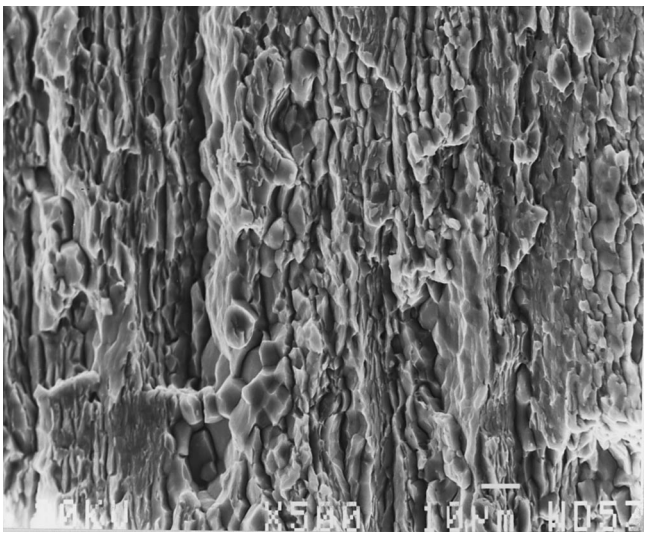

Fig. 13—SEM fractograph of Al-Cu-Li-In, longitudinal orientation, T6 temper.

$$\varepsilon = \frac{1}{3}\left(\frac{1+\nu}{1-\nu}\right)\delta \qquad [7]$$

where δ is the lattice misfit strain at the particle-matrix

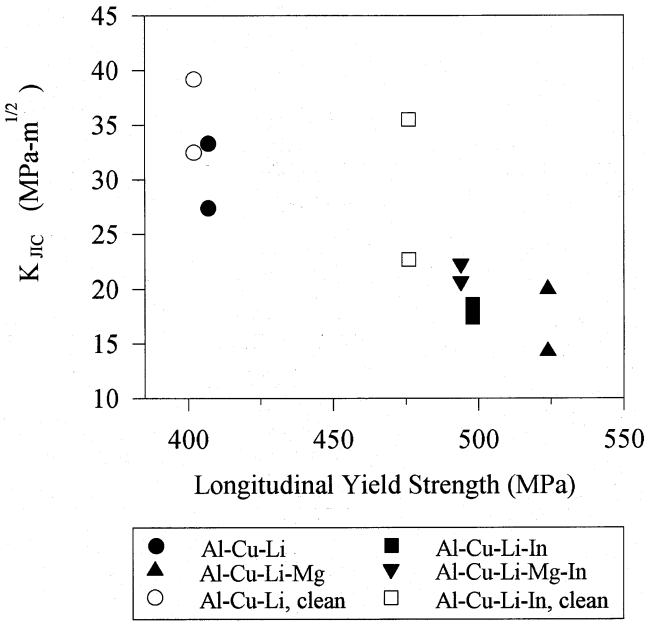

Fig. 14—K_{JIC} plane-strain fracture initiation toughness *vs* yield strength for L-T oriented sheet material, all samples T6 temper.

Table VII. Yield Model Input Data

Alloy	Time	V_v (Pct) {100}	V_v (Pct) T_1	*d, t* (nm) {100}	*d, t* (nm) T_1	Yield Strength (MPa) σ_{YS}	Yield Strength (MPa) σ_{AQ}	M
Al-Cu-Li	5	1.7	—	34, 0.8	—	206	152	3.20
	20	1.9	—	68, 1.2	—	270	152	3.20
	48	3.2	—	77, 1.8	—	317	152	3.20
+In	5	2.1	0.4	36, 1.3	46, 2.3	296	145	3.14
	20	2.7	1.0	59, 2.4	83, 2.2	482	145	3.14
	48	4.9	1.2	63, 2.2	77, 2.0	494	145	3.14
+Mg	5	1.3	0.1	28, 1.5	28, 2.0	300	160	3.16
	20	2.1	1.6	45, 1.8	115, 2.6	390	160	3.16
	48	1.8	1.9	59, 2.6	164, 3.0	462	160	3.16
+Mg + In	5	2.0	0.6	22, 0.8	48, 1.4	300	157	3.25
	20	2.3	2.4	43, 2.5	120, 2.5	366	157	3.25
	48	2.8	3.0	65, 1.9	190, 2.5	450	157	3.25

Times given are for hours of aging at 160 °C.

interface. As this model was developed for shearing of spherical precipitates, it was used with δ as a curve-fitting parameter. The best fit to the data was achieved for a δ value of 0.9 pct. This is not far from experimental values measured by Stobbs and Purdy[40] or calculated theoretically by Dahmen and Westmacott.[41]

3. *Yield model results*

The strengthening components of the looped θ' and T_1 phases were combined by a Pythagorean addition law. This is empirically found to give the best fit for combinations of particles with similar strengths. The Orowan model and coherency strain model results were combined with an exponential addition law with an exponent of 1.4, which has been found to give the best empirical fit for combinations of strong and weak particles.[42] Thus, the total predicted increment of shear strength due to the presence of precipitates is

Table VIII. Yield Model Results

Composition	Time	L_0 (θ'/T_1)	$\Delta\tau_{shear}$	$\Delta\tau_{\theta'}$	$\Delta\tau_{T_1}$	$\Delta\tau_{pred}$	$\Delta\tau_{exp}$
Al-Cu-Li	5	—/—	49	—	—	49	53
	20	—/—	73	—	—	73	73
	48	—/—	100	—	—	100	88
+In	5	—/118	56	—	37	77	83
	20	40/80	—	118	60	131	142
	48	21/64	—	219	73	232	146
+Mg	5	—/188	39	—	21	50	81
	20	—/69	62	—	75	113	109
	48	58/70	—	83	81	115	132
+Mg + In	5	—/70	42	—	58	82	78
	20	—/46	64	—	113	147	99
	48	33/30	—	140	186	233	125

Times are for hours of aging at 160 °C. The value of L_0 is in nanometers. All strengths are in MPa.

$$(\Delta\tau_{pred})^{1.4} = (\Delta\tau_{shear})^{1.4} + (((\Delta\tau_{\theta'})^2 + (\Delta\tau_{T1})^2)^{0.5})^{1.4} \quad [8]$$

As stereological data were taken at three different stages of aging at 160 °C (433 K), assumptions were made (based upon TEM observations and yield behavior) regarding when the transition from shearing to looping of the {100} phases occurs in each alloy. Precipitates in the baseline alloy were assumed to be sheared for all three times studied. Al-Cu-Li-In was assumed to have {100} precipitates undergoing shearing at 5 hours, then looping thereafter. The two Mg-containing alloys were assumed to have {100} particles shearing at 5 and 20 hours, looping at 48 hours. The T_1 was assumed to be looped by dislocations at all stages of aging.

Table VII summarizes the microstructural data input into the preceding models, while Table VIII gives the results. Interparticle spacings are given for looped particles only, as the shear model used here does not give a readily interpretable spacing. The polycrystalline experimental data must be converted in order to make valid comparisons with the model:

$$\Delta\tau_{exp} = (\sigma_{YS} - \sigma_{matrix}) \div M \quad [9]$$

where M is the Taylor factor for the given alloy, calculated from texture data.

The results show that this model is reasonably successful at predicting longitudinal yield strengths from precipitate stereology data. There are several possible sources of error. First, T_1 strengthening may be overstated, especially in the Mg alloys where the plates tended to be associated to some extent with dislocations and subgrains, thus giving a higher effective spacing than if they were distributed more homogeneously throughout the matrix. Additionally, it is possible that T_1, which is assumed always to be looped, is instead sheared in some regions due to planar slip created by shearing of θ'' particles.[8]

However, the most likely source of error in the model is associated with the precipitate volume fractions measured by stereology. While the point count method used for measuring projected areal fractions is theoretically the most accurate, it is subject to sizable uncertainties when the particles measured are as small in one dimension as the precipitate plates were. Simple calculations show that the total volume fraction of precipitates should be from 3.8 to 4.4 pct, given that Cu concentration is the limiting factor

Table IX. Anisotropy Model Results

Composition	Model (G_p/30) σ_{45} deg/σ_0 deg, σ_{90} deg/σ_0 deg	Model (Curve Fit) σ_{45} deg/σ_0 deg, σ_{90} deg/σ_0 deg	Measured σ_{45} deg/σ_0 deg, σ_{90} deg/σ_0 deg
Al-Cu-Li-In	1.01, 1.02	0.97, 0.98	0.970, 0.978
Al-Cu-Li-Mg	0.97, 1.00	0.98, 0.98	0.938, 0.985
Al-Cu-Li-Mg-In	0.96, 0.96	0.94, 0.95	0.942, 0.989

Table X. Vacancy-Solute Binding Energies in Aluminum Alloys[25,50,51]

Solute Element	Vacancy Binding Energy (eV)
Mg	0.45*, 0.19, 0.36
Li	0.26
In	0.20*, 0.25
Zr	0.24, 0.30
Si	0.23, 0.22
Cd	0.18
Cu	0.05, 0

All data are from binary alloys except for those marked with an asterisk, which are from Al-4Cu ternaries.[50]

for the formation of θ' (Al_2Cu) and T_1 (Al_2CuLi). The cases that display the greatest discrepancy between the predicted and measured strength values (Al-Cu-Li-In, 48 hours, and Al-Cu-Li-Mg-In, 20 and 48 hours) have precipitate volume fractions of 6.1, 4.7, and 5.8 pct, respectively.

B. *Anisotropy Modeling*

Based upon the work of Hosford and Zeisloft[3] (HZ), Bate *et al.*[43,44] (BRW) proposed a continuum model of polycrystalline anisotropy that considers the interaction between oriented precipitates and the macroscopic texture of the material. The HZ model maintains compatibility between the matrix and precipitate phases by a combination of plastic deformation and rotation of the particles, assuming constant stress within the strengthening phase. The BRW model assumes that the precipitates undergo an elastic deformation that does not depend upon position within the particle, similar to an Orowan strengthening mechanism, and compatibility is maintained by the generation of an accommodation strain in the particle and a back stress in the matrix phase.[45,46] The polycrystalline yield strength is then given by

$$\sigma_y = (1 - V_v)\ \tau M + 2V_v\ G_m\ \|\gamma\|\ \varepsilon_p \qquad [10]$$

where τ is the matrix shear strength (calculated as described in Section A), γ is the Eshelby accommodation tensor (subscripts not written out), and ε_p is the strain discontinuity at the precipitate-matrix interface. The term $2G_m\varepsilon_p$ is an adjustable precipitate back-stress parameter analogous to the precipitate strength, σ_p, in the HZ[3] model, and $\|\gamma\|$ is analogous to $\overline{N}$. Volume fractions used are given in Table VII.

Given the weighted coefficients of the ODF for an alloy from the popLA software package and knowing the precipitate habit planes, it was possible to calculate $\|\gamma\|$ averaged over all grain orientations as a function of the tensile axis orientation relative to the rolling direction using a computer program developed by Lyttle and Wert.[31] The shape of the $\|\gamma\|$ curve for plates with {111} habit planes is similar to that of the Taylor factors in Figure 2, indicating that these precipitates will tend to reinforce the rolling texture anisotropy. Conversely, $\|\gamma\|$ is highest near 45 deg to the rolling direction for plates with {100} habit planes which therefore tend to weaken the original texture anisotropy. The {100} rods are calculated and observed experimentally to behave in a fashion similar to {100} plates.[4,5]

Table IX gives the anisotropies predicted by Eq. [10] for the alloys after aging for 48 hours at 160 °C (433 K), where strengthening is controlled by Orowan looping. Experimental anisotropies are given for the T6 temper. Model results are first given using the dislocation-free yield strength of the precipitate, G_p/30, as an estimate for $2G_m\ \varepsilon_p$. O'Dowd and co-workers[47,48] calculated the Young's modulus of the T_1 phase to be 320 GPa, and Fouquet *et al.*[49] calculated the Young's modulus of the θ' phase to be 120 GPa. Assuming that the matrix and precipitates have the same Poisson's ratio, the shear moduli are calculated to be 119 and 44 GPa, respectively. The corresponding values of G_p/30 are 4.0 and 1.5 GPa for T_1 and θ'. Results are also given using $2G_m\ \varepsilon_p$ as a least-squares curve-fitting parameter, which gives values of roughly 23 and 1.7 GPa for T_1 and θ', respectively. Bate *et al.*[43,44] calculate the θ' back stress to be 3 or 5.5 GPa, depending on whether plastic or elastic particle deformation is assumed. The agreement between the model and the limited experimental data is reasonably good.

In hindsight, this alloy system was not an ideal test case for anisotropy modeling, as the measured anisotropies are not large. However, the model does a good job of predicting the relative effects of the θ' and T_1 precipitates on anisotropy. In addition, the deleterious effect of T_1 on anisotropy may be greater than this simple model would indicate if one accounts for the higher aspect ratio of the T_1 particles relative to θ' in the Mg-containing alloys.[32] The trends of the measured anisotropies agree well with the preceding model. The Mg-free alloys, strengthened predominantly by θ'' and θ', have very low anisotropies. The Mg-containing alloys, which have larger amounts of high-aspect ratio T_1 plates, have larger anisotropies. The largest anisotropies which were measured were those for the Mg-containing alloys in the T86 temper, in which T_1 overwhelmingly outnumbers θ'.

C. *Trace Element Effects*

1. *Vacancy interactions*

Vacancy-solute binding energies in binary aluminum alloys are shown in Table X.[25,50,51] Where two figures are shown, the latter is the more recent measurement. While many of the solute elements in the alloys studied here are known to have significant interaction with vacancies, Mg has the highest binding energy and is also present in much higher concentrations than In or Zr. The experimental evidence in this study indicates that Mg affects the precipita-

tion kinetics of the {100} Al-Cu phases *via* a vacancy interaction mechanism. The as-quenched microstructures, natural aging behavior, data from aging at 120 °C (393 K), and direct-to-aging-temperature quench data all indicate that Mg binds with vacancies and produces a high density of GP zones and θ'' precipitates. This high number density of fine shearable particles is responsible for the accelerated aging observed in the Mg-bearing alloys at room temperature and 120 °C (393 K), as well as the increase in yield strength *vs* the baseline alloy after aging for 5 hours at 160 °C (433 K).

The exact process by which this vacancy interaction would affect precipitation is not known, but a vacancy-pump mechanism is possible.[52] This increases the rate of diffusion and, in turn, enhances nucleation and growth kinetics. A high Mg-vacancy binding energy may also directly increase the concentration of vacancies at the solutionizing temperature.[51] Magnesium atoms and vacancies may also associate with Cu solute atoms, creating highly mobile Mg-Cu-vacancy clusters.[50,53,54] This would increase Cu diffusion rates and thus assist the nucleation of GP zones during low-temperature aging. These clusters should be distributed fairly homogeneously throughout the matrix, resulting in a high number density of GP zones. Unfortunately, such preliminary clustering would be difficult to observe, as GP zone formation would lead to the dissolution or incorporation of the original nuclei.

Indium-vacancy interactions have been hypothesized to cause the suppression of natural aging by In in Al-Cu alloys.[50] However, this effect was not observed in the present work. It seems likely that, as Li and In have similar vacancy binding energies in binary aluminum alloys and the concentration of Li is roughly 250 times greater than that of In, there is no significant In-vacancy interaction in this alloy system. The fact that Mg does display such an interaction may be attributed to its higher vacancy binding energy and that it is present in solution at a concentration some 30 times higher than that of In.

2. *Magnesium effects on T_1 precipitation*

The reason for enhancement of T_1 precipitation by Mg is not as clear as the reason for its effects on GP zones and θ''. Noble and Thompson[55] concluded that high Cu content, high vacancy concentrations, and GP zones are all conducive to a homogeneous distribution of T_1 precipitates in the matrix. As previously noted, these features are all present in the Mg-containing alloys in this study. Itoh *et al.*[56] reported nucleation of T_1 at three sites in an Al-4Cu-1.1Li-0.4Mg-0.2Zr sheet alloy aged for 40 minutes at 180 °C (453 K): on dislocation loops associated with Al_3Zr particles, at octahedral voids formed by vacancy condensation, and as {111} GP zones which were enriched in Mg and Cu. The presence of Mg in a T_1 GP zone would partially counteract the strain associated with the Cu atoms. As monolithic Mg has an hcp crystal structure, trace Mg additions might also stabilize the T_1 hcp crystal structure or stabilize stacking faults, thought to act as nucleation sites for this phase.[54,57] However, no anomalous Mg concentrations were found in energy dispersive spectroscopy microanalysis of T_1 plates in the present study.

The addition of Mg to the baseline alloy increases the density of dislocation loops in the as-quenched microstructure, and at later stages of aging, T_1 plates are observed to be associated with dislocations in some areas of the Mg-bearing alloys, which agrees with the results of Cassada *et al.*[57] The T_1 is also seen at subgrain boundaries in the baseline alloy, especially at longer aging times, but in much smaller quantities. It is possible that the dislocation helices may be better heterogenous nucleation sites for T_1 than the subgrain boundary dislocations. This difference may be enhanced due to the accelerated growth kinetics in the Mg-bearing alloys as discussed previously. This would explain the relatively low number densities and coarse morphologies of T_1 in the Mg-based alloys and why T_1 seems to be associated more with dislocations in these alloys than in Al-Cu-Li-In.

The effect of Mg on the T8 microstructure may also be seen in terms of enhanced growth kinetics. The TEM observations indicate that the baseline alloy is in the metastable θ' plus T_1 phase field, but T_1, normally considered an equilibrium phase, is not seen to occur in significant amounts in the matrix, indicating that its formation is kinetically limited. This is in agreement with the X-ray data of Silcock,[21] which show that the T_1 reflections in an Al-4Cu-1.2Li alloy aged for 16 hours at 165 °C (438 K) are very weak. In the T8 condition, the baseline alloy contains an increased amount of T_1. The T8 Mg-containing alloys are strengthened almost entirely by T_1. It appears that the barrier to T_1 precipitation in the baseline alloy is kinetic in nature, and in order to appear in significant amounts within a reasonable aging time, it requires aid both in nucleation and in growth. In the T8 condition, the dislocation jogs provide the nucleation sites, and Mg-vacancy interactions enhance the growth kinetics.

3. *Indium*

Indium effects precipitation in two ways: by increasing the thickness of the {100} plates during the early stages of aging and later by promoting more homogeneous precipitation of T_1 in the matrix. It seem likely that the change in θ'/θ'' morphology causes the early acceleration of aging while the particles are sheared by dislocations. The Al-Cu-Li-In alloy displayed a considerable degree of strain localization in samples aged for 5 hours at 160 °C (433 K). This agrees with the calculations of Duva *et al.*,[58] which show that strain localization increases with increasing particle size as long as the particles are sheared. The appearance of T_1 as aging proceeds then shifts the mode of dislocation-precipitate interaction to looping, providing the final increment of strengthening. The various underlying mechanisms by which In might cause these changes, outlined in Section I, will be considered individually.

Several authors[2,14,15,59] have concluded that In precipitates out of the matrix as fine spherical particles during the early stages of aging. These particles would then act as heterogeneous nucleation sites for the θ' or T_1 phase. No In-rich particles were found to be associated with any precipitates in this work. The discrepancy may be due to the difference in aging temperature; the previously published results were for samples aged between 190 °C (463 K) and 250 °C (523 K) for several minutes to several hours. The presence of Li may also interfere with the formation of trace element particles, as Silcock[21] found that the *Cd*' precipitate phase observed in X-ray data from Al-Cu-Cd alloys was not observed in Al-Cu-Li-Cd alloys. It should also be noted that only the work of Mukhopadhyay in an Al-Cu-

Mg-In alloy[59] has clearly shown the existence of In precipitates in the matrix prior to the formation of the strengthening phases. It may be in some cases that In precipitates onto the θ' or T_1 plates, not *vice versa*. Alternatively, it may be that In is originally present at precipitate ledge growth interfaces in concentrations which were not detectable in this study, and only at later stages of aging does it accumulate at the plate edges as an In-rich particle.

Any substantial changes in the volume free energy, strain energy, or precipitate interfacial energies would require trace element segregation, whether throughout the precipitate structure or just at the particle-matrix interface. Assuming that all of the In is associated with θ' particles, one can calculate what concentrations would be present. If the In is spread evenly throughout the precipitate, the Al-Cu-Li-In stereology data for 5 hours aging at 160 °C (433 K) would give the concentration as ~1 at. pct. If one assumes that the In is confined to a 1-atom-deep layer at the precipitate-matrix interface, the concentration would be ~5 to 6 at. pct. Corresponding calculations assuming all of the In is in the T_1 plates would give concentrations of 3 and 36 at. pct, respectively. As detailed earlier, the microanalysis resolution for In was estimated to be 0.4 at. pct.

It would seem that, given the preceding calculations, In segregation should have been detected if present. However, Silcock[60] estimated the solubility of In in Al at 530 °C (803 K) to be 0.05 wt pct, considerably less than the alloy concentration of 0.09 wt pct used in the previous calculations. If it is assumed that this is the amount of In in the matrix, then the volume or interfacial concentrations after 5 hours at 160 °C (433 K) would be 0.5 at. pct in the precipitate or 3.5 at. pct at the interface if concentrated in the θ' phase, or 2 at. pct in the precipitate or 22.5 at. pct at the interface if concentrated in the T_1 phase. In light of these figures, it is certainly possible that In could be present in the θ' particles without being detected. The fact that θ' coarsening rates in the Al-Cu-Li-In alloy are slow compared with those in the other alloys would also seem to imply that In is segregated to the precipitates in some manner.

Indium was not seen to accelerate aging or improve strength in the presence of Mg. Most likely this is due to the fact that, with 30 times more Mg atoms than In atoms, the effect of Mg dilutes that of In. That is, since the Mg enhances the precipitation of the θ'' phase and greatly increases its number density during the early stages of aging, there may not be enough In per precipitate to reach some critical level at which the morphology is effected.

The Al-Cu-Li-In alloy does not benefit significantly from cold work prior to aging. As the T8 Al-Cu-Li-In alloy resembles the T8 baseline alloy closely not only in strength, but in microstructure as well, it seems that In is somehow immobilized or neutralized by a high dislocation density. Hardy[61] observed that the peak hardness of a ternary Al-Cu-In alloy actually decreased somewhat when cold work was applied prior to aging. He hypothesized that, due to their relatively large size, In atoms are trapped in areas of tensile strain at dislocations. Silcock[21] found that, in an Al-4Cu-1.2Li-0.1Cd alloy (wt pct), a 5 pct stretch had slightly positive effects on aging. It may be that, in Al-Cu-Li, the dislocations in the T8 temper serve as heterogeneous nucleation sites for θ' precipitation to such an extent that In, which enhances θ' precipitation in the T6 condition, has no role to play, but the Li content ensures enough T_1 precipitation on jogs to keep the T8 strength level from falling relative to the T6 temper.

4. *Silicon*

The role that Si plays as an impurity in this alloy system is not clear. It is known that Si can bind with vacancies, and it is thought to interact with Mg in Al-Cu-Mg alloys to form Mg_2Si in some cases.[62] The low-Si alloys studied did display the beneficial In effect on the peak hardness level, but the aging time necessary to achieve peak strength was increased relative to the conventional-purity Al-Cu-Li-In. It is possible that Si has a beneficial interaction with In in the conventional-purity alloy. However, the low-Si precipitate microstructures were coarser, and more T_1 was observed in the low-Si baseline alloy. This suggests that the levels of Si present in the conventional-purity (roughly twice the level of In present) retard the growth of the strengthening precipitates in some way. The growth kinetics in the vacuum-refined alloys would thus be enhanced, but if the number of heterogeneous nucleation sites is reduced by the removal of impurities, then age hardening will proceed more slowly than in the conventional-purity alloys. Quenching experiments did not indicate any significant solute-vacancy interactions nor did the natural aging behavior for the low-Si alloys differ from their conventional-purity counterparts.

The hardness curves and yield data for the low-impurity alloys contained much more variability than the conventional-purity sample data. The clean alloys were cast under a different process than the original four alloys, and while they were nominally subjected to identical rolling schedules, it is possible that some behavior in these alloys is due to thermomechanical effects rather than compositional ones.

D. *Fracture Behavior*

Wagner and Gangloff[63] found that 0.15 wt pct addition of In to 2090 caused the fracture toughness to decrease significantly, with intersubgranular failure predominating. This is not surprising, recalling that 0.05 wt pct is believed to be the solubility of In in aluminum at a solutionizing temperature of 530 °C (803 K).[60] Although the present alloys contain approximately 0.08 wt pct In, intersubgranular fracture was not seen to any significant extent in longitudinal tensile testing of the sheet material. The In concentrations present in the alloys in this study do not seem to have a deleterious effect on fracture toughness, even though the solubility limit may be exceeded somewhat at the solution heat treatment temperature. The reductions in toughness that are observed are not greater than would be expected for the strength increase that In provides.

As has been previously reported,[26] lowering the levels of impurities such as Na and K does improve fracture properties in this alloy system. This effect is most significant when the conventional-purity alloys have low ductilities, such as for transverse tensile testing in the sheet material. This may be understood as a ''weak-link'' effect. That is, if there are high resolved stress states normal to the grains or along grain boundaries, impurities at the boundaries will cause failure. If the stresses are mostly parallel to the grain boundaries, as for longitudinal tensile testing in these alloys

which display an unrecrystallized rolling texture, the impurity levels will have a relatively small effect on ductility or fracture toughness. The results of this study support the contention that lowering the Na and K levels can improve ductility in certain orientations in Al-Li alloys.

V. CONCLUSIONS

Trace additions of In increased the T6 yield strength of the Al-Cu-Li alloy studied by 25 pct. The T6 strength of the Al-Cu-Li-In alloy was roughly equal to that of the T86 Al-Cu-Li. Cold work before aging did not increase the strength of the Al-Cu-Li-In alloy. The aging time required to reach peak strength in the Al-Cu-Li-In alloy was only one-quarter that for the baseline alloy. The increase in strength is due at early stages of aging to the increase in thickness of the θ'' precipitates, which are sheared. This also causes strain localization in underaged samples. At peak strength, the transition from particle shearing to Orowan looping is promoted by matrix precipitation of the T_1 phase, which provides a secondary strengthening effect, although it is present in smaller volume fractions than θ''. Indium particles were not found in the matrix or in association with strengthening phases. No significant In-vacancy interactions were seen. Experimental results seem to indirectly indicate that In segregates to precipitates, but no such segregation was detected within the resolution limits of the TEM X-ray microanalysis system used.

An addition of 0.5 wt pct Mg to the baseline alloy increased the T6 yield strength of the baseline alloy by 30 pct. The increase in strength in the early stages of aging is primarily due to the precipitation of a high number density of fine θ'' and GP zone phases. Magnesium enhances precipitation kinetics by interaction with quenched-in vacancies. As aging proceeds, significant amounts of high-aspect ratio T_1 grow, especially near dislocations and subgrain boundaries. Nucleation of T_1 may be aided by the presence of dislocation loops and helices condensed from quenched-in vacancies. No anomalous Mg concentrations were found in any part of alloy microstructures. The T86 temper of the Mg-bearing alloys is strengthened entirely by T_1. The increased volume fraction of $\{111\}$ precipitates in the Mg-bearing alloys leads to a higher degree of yield anisotropy, in agreement with theoretical models. Little difference was noted in mechanical properties or microstructure when In was added to the Al-Cu-Li-Mg alloy.

The beneficial effects of Mg in the Al-Cu-Li system seem to be greatest when the growth kinetics of the original alloy are slow, such as for aging at low temperatures. High Cu levels may also be necessary, as Mg and Cu may associate during the formation of GP zones. High levels of Li may interfere with the Mg effect as they compete for vacancies; alloys which are significantly strengthened by δ' would not be expected to experience a large Mg effect on aging.

Removal of low-level Si impurities did not influence the magnitude of the In strength increase, but did seem to slow aging kinetics. The microstructures were similar to those in the higher-Si alloys, but precipitates were larger, with higher aspect ratios, and more T_1 was present. No Si-vacancy interactions were observed. Results for the low-impurity alloys were difficult to interpret due to large variability in the data, but a nonzero level of Si (below that which would have a deleterious effect on fracture toughness) may be desirable.

The In and Mg additions did not reduce the fracture toughness of the baseline alloy more than would be expected for the accompanying strength increases. Reducing alkali metal impurity levels did not increase the fracture toughness significantly in the L-T oriented plate but did improve the tensile ductility of the sheet at 45 and 90 deg to the rolling direction. The K_{JIC} values for the L-T oriented sheet were also significantly higher in the clean alloys.

ACKNOWLEDGMENTS

The authors thank the Office of Naval Research for providing funding under Contract No. N00014-91-J-1285, George Yoder, contract monitor. One of the authors (DLG) also received support from the National Science Foundation in the form of a Graduate Research Fellowship. Thanks are also due to Dr. Hinrich Hargarter, who provided the strain localization micrographs.

REFERENCES

1. I.J. Polmear: *Light Alloys: Metallurgy of the Light Metals*, 2nd ed. Edward Arnold, New York, NY, 1989.
2. A.K. Mukhopadhyay, G.J. Shiflet, and E.A. Starke, Jr.: *Morris E. Fine Symp.*, P.K. Liaw, J.R. Weertman, H.L. Marcus, and J.S. Santner, eds., TMS, Warrendale, PA, 1991, p. 283.
3. W.F. Hosford and R.H. Zeisloft: *Metall. Trans.*, 1972, vol. 3, pp. 113-21.
4. M.A. Przystupa, A.K. Vasudevan, and W.G. Fricke, Jr.: *8th Int. Conf. on Textures of Materials*, J.S. Kallend and G. Gottstein, eds., TMS, Warrendale, PA, 1988, p. 1051.
5. A.K. Vasudevan, W.G. Fricke, Jr., M.A. Przystupa, and S. Panchanadeeswaran: *8th Int. Conf. on Textures of Materials*, J.S. Kallend and G. Gottstein, eds., TMS, Warrendale, PA, 1988, p. 1071.
6. A.K. Vasudevan, M.A. Przystupa, and W.G. Fricke, Jr.: *Scripta Metall.*, 1990, vol. 24, p. 1429.
7. A.K. Vasudevan and M.A. Przystupa: *Aluminum-Lithium Alloys for Aerospace Applications Workshop*, NASA Conference Publication No. 3287, B.N. Bhat, T.T. Bales, and E.J. Vesely, Jr., eds., NASA, Washington, DC, 1994.
8. C.P. Blankenship, Jr., E. Hornbogen, and E.A. Starke, Jr.: *Mater. Sci. Eng.*, 1993, vol. A169, p. 33.
9. A.H. Sully, H.K. Hardy, and T.J. Heal: *J. Inst. Met.*, 1949, vol. 76, p. 269.
10. H.K. Hardy: *J. Inst. Met.*, 1950–51, vol. 78, p. 169.
11. H.K. Hardy: *J. Inst. Met.*, 1951–52, vol. 80, p. 483.
12. J.D. Boyd and R.B. Nicholson: *Acta Metall.*, 1971, vol. 19, p. 1101.
13. J.M. Silcock: *Phil. Mag.*, 1959, vol. 8, p. 1187.
14. R. Sankaran and C. Laird: *Mater. Sci. Eng.*, 1974, vol. 14, p. 271.
15. H. Suzuki, M. Kanno, and K. Fukunaga: *J. Jpn. Inst. Light Met.*, 1975, vol. 25, p. 413.
16. J.B.M. Nuyten: *Acta Metall.*, 1967, vol. 15, p. 1765.
17. J.M. Silcock, T.J. Heal, and H.K. Hardy: *J. Inst. Met.*, 1955–56, vol. 84, p. 23.
18. S.P. Ringer, K. Hono, and I.J. Polmear: *4th Int. Conf. on Aluminum Alloys*, T.H. Sanders, Jr. and E.A. Starke, Jr., eds., Georgia Institute of Technology, Atlanta, GA, 1994, vol. 1, p. 574.
19. E.H. Spuhler: *Alcoa Alloy X2020*, Aluminum Company of America Green Letter, Alcoa, Alcoa Center, PA, Sept. 1958.
20. I.M. LeBaron: U.S. Patent No. 2,381,219, 1945.
21. J.M. Silcock: *J. Inst. Met.*, 1959–60, vol. 88, p. 357.
22. L. Blackburn and E.A. Starke, Jr.: in *Aluminum-Lithium Alloys V*, E.A. Starke, Jr. and T.H. Sanders, Jr., eds., MCEP, Birmingham, United Kingdom, 1989, p. 751.
23. R.K. Wyss and R.E. Sanders, Jr.: *Metall. Trans. A*, 1988, vol. 19A, pp. 2523-30.
24. W.K. Armitage: *J. Inst. Met.*, 1970, vol. 98, p. 46.

25. J.J. Regidor and A. Sanchez: *6th Int. Light Metals Congr.*, Aluminium-Verlag GMBH, Düsseldorf, Germany, 1975, p. 29.
26. C.G. Bennett and D. Webster: *4th Int. Conf. on Aluminum Alloys*, T.H. Sanders, Jr. and E.A. Starke, Jr., eds., Georgia Institute of Technology, Atlanta, GA, 1994, p. 98.
27. E.E. Underwood: *Quantitative Stereology*, Addison-Wesley, Reading, MA, 1970.
28. B.W. Williams: *Practical Analytical Electron Microscopy in Materials Science*, Verlag Chemie International, New York, NY, 1984.
29. U.F. Kocks, J.S. Kallend, H.R. Wenk, A.D. Rollett, and S.I. Wright: popLA-Preferred Orientation Package-Los Alamos, Los Alamos National Laboratory, Los Alamos, NM, July, 1994.
30. M.J. Haynes and R.P. Gangloff: *J. Test. Eval.*, vol. 25, 1996, p. 82.
31. M.T. Lyttle and J.A. Wert: *Metall. Mater. Trans. A*, 1996, vol. 28A, p. 3503.
32. J.F. Nie, B.C. Muddle, and I.J. Polmear: *5th Int. Conf. on Aluminium Alloys*, part 2, J.H. Driver, B. Dubost, F. Durand, R. Fougeres, P. Guyot, P. Sainfort, and M. Suery, eds., appeared in *Mater. Sci. Forum*, 1996, vols. 217–222, p. 1257.
33. L.M. Brown and R.K. Ham: *Strengthening Methods in Crystals*, A. Kelly and R.B. Nicholson, eds., Wiley, New York, NY, 1971, p. 12.
34. L.F. Mondolfo: *Aluminum Alloys*, Butterworth and Co., London, 1979, p. 69.
35. B. Noble, S.J. Harris, and K. Dinsdale: *Met. Sci.*, 1982, vol. 16, p. 425.
36. S.J. Harris, B. Noble, and K. Dinsdale: *4th Int. Aluminium Lithium Conf.*, G. Champier, B. Dubost, D. Miannay, and L. Sabetay, eds., Les Editions Physique, Les Ulis, France, 1987, pp. C3-415.
37. P.M. Kelly: *Scripta Metall.*, 1972, vol. 6, p. 647.
38. P. Merle, F. Fouquet, and J. Merlin: *Mater. Sci. Eng.*, 1981, vol. 50, p. 215.
39. J.C. Huang and A.J. Ardell: *4th Int. Aluminium Lithium Conf.*, G. Champier *et al.*, eds., Les Editions Physique, Les Ulis, France, 1987, pp. C3-373.
40. W.M. Stobbs and G.R. Purdy: *Acta Metall.*, 1978, vol. 26, p. 1069.
41. U. Dahmen and K.H. Westmacott: *Phys. Status Solidi. A*, 1983, vol. 80, p. 249.
42. A.J. Ardell: *Metall. Trans. A*, 1985, vol. 16A, pp. 2131-65.
43. P. Bate, W.T. Roberts, and D.V. Wilson: *Acta Metall.*, 1981, vol. 29, p. 1797.
44. P. Bate, W.T. Roberts, and D.V. Wilson: *Acta Metall.*, 1982, vol. 30, p. 725.
45. J.D. Eshelby: *Proc. R. Soc.*, 1957, vol. A241, p. 376.
46. L.M. Brown and W.M. Stobbs: *Phil. Mag.* 1971, vol. 23, p. 1185.
47. M.E. O'Dowd: Ph.D. Dissertation, University of Virginia, Charlottesville, VA, 1987.
48. M.E. O'Dowd, W. Ruch, and E.A. Starke, Jr.: *4th Int. Aluminium Lithium Conf.*, G. Champier *et al.*, eds., Les Editions Physique, Les Ulis, France, 1987, pp. C3-565.
49. F. Fouquet, P. Merle, M. Kohen, J. Merlin, and P.F. Gobin: *Acta Metall.*, 1979, vol. 27, p. 315.
50. K.M. Entwistle, J.H. Fell, and K.I. Koo: *J. Inst. Met.*, 1962–63, vol. 91, p. 84.
51. S. Özbilen and H.M. Flower: *Acta Metall.*, 1989, vol. 37, 2993.
52. A.J. Perry: *Acta Metall.*, 1966, vol. 14, p. 1143.
53. A. Garg and J.M. Howe: *Acta Metall.*, 1991, vol. 39, p. 1925.
54. S. Hirosawa, T. Sato, A. Kamio, K. Kobayashi, and T. Sakamoto: *4th Int. Conf. on Aluminum Alloys*, T.H. Sanders, Jr. and E.A. Starke, Jr., eds., Georgia Institute of Technology, Atlanta, GA, 1994, vol. 2, p. 199.
55. B. Noble and G.E. Thompson: *J. Met. Sci.*, 1972, vol. 6, p. 167.
56. G. Itoh, Q. Cui, and M. Kanno: *Mater. Sci. Eng.*, 1996, vol. A211, p. 128.
57. W.A. Cassada, G.J. Shiflet, and E.A. Starke, Jr.: *Metall. Trans. A*, 1991, vol. 22A, pp. 287-97.
58. J.M. Duva, M.A. Daeubler, E.A. Starke, Jr., and G. Lütjering: *Acta Metall.*, 1988, vol. 36, p. 585.
59. A.K. Mukhopadhyay, K.S. Prasad, and C.R. Chakravorty: *5th Conf. on Aluminium Alloys*, part 2, J.H. Driver *et al.*, eds., appeared in *Mater. Sci. Forum*, 1996, vols. 217–222, p. 753.
60. J.M. Silcock: *J. Inst. Met.*, 1955–56, vol. 84, p. 19.
61. H.K. Hardy, *J. Inst. Met.*, 1954–55, vol. 83, p. 337.
62. G.B. Brook and B.A. Hatt: *The Mechanism of Phase Transformations in Crystalline Solids*, Monograph No. 33, The Institute of Metals, London, 1969, p. 82.
63. J.A. Wagner and R.P. Gangloff: *Scripta Metall.*, 1992, vol. 26, p. 1779.